Interfacial electron redistribution allows advanced phosphate adsorption in Zn/La-loaded magnetic mesoporous nanospheres

He, Fanglin; Chang, Ming; Wei, Chaohai; Qian, Feng; Deng, Xuhan; Qiu, Guanglei

DOI
10.1016/j.watres.2025.124753

Publication date
2025

Document Version
Final published version

Published in
Water Research

Water Research 288 (2026) 124753

Contents lists available at ScienceDirect

Water Research

journal homepage: www.elsevier.com/locate/watres

Interfacial electron redistribution allows advanced phosphate adsorption in Zn/La-loaded magnetic mesoporous nanospheres

Fanglin He [a], Ming Chang [b], Chaohai Wei [a,c,d], Feng Qian [e], Xuhan Deng [f], Guanglei Qiu [a,c,d,e,*]

[a] School of Environment and Energy, South China University of Technology, Guangzhou 510006, China
[b] Guangdong-Hong Kong-Macao Research Center for Ecology and Environmental Science, Guangzhou 510530, China
[c] Key Laboratory of Pollution Control and Ecological Restoration in Industrial Clusters, Ministry of Education, Guangzhou 510006, China
[d] Guangdong Provincial Key Laboratory of Solid Wastes Pollution Control and Recycling, Guangzhou 510006, China
[e] National Joint Research Center for Ecological Conservation and High-Quality Development of the Yellow River Basin, Beijing 100018, China
[f] Faculty of Civil Engineering and Geosciences, Delft University of Technology, Delft 2028, Netherland

HIGHLIGHTS

- A novel Zn/La bimetallic magnetic mesoporous silica composite was developed.
- Achieving a maximum phosphate adsorption capacity of 140.9 mg P/g.
- Zn achieves d-orbital hybridization with La and triggers interfacial electron redistribution.
- Enabling unprecedented phosphate adsorption and inspiring new design principles.

GRAPHICAL ABSTRACT

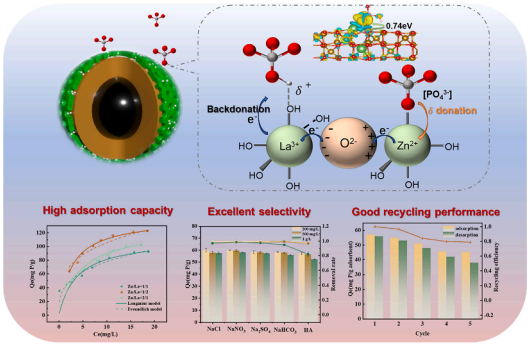

ARTICLE INFO

Keywords:
Functionalized magnetic mesoporous microspheres
Phosphate
Adsorption
Bimetallic synergetic effects, interfacial electron redistribution

ABSTRACT

A core-shell structured Zn/La magnetic mesoporous silica (denoted as Zn/La-MMS) composite we successfully constructed via etching and co-deposition techniques, achieving exceptionally efficient adsorption of phosphate. At an optimized Zn/La ratio of 0.5 (i.e., Zn/La-0.5 MMS), the composite exhibited an ordered mesoporous structure and superior adsorption performance with a maximum phosphate adsorption capacity of 140.9 mg P/g (15-fold higher than the pristine MMS). High adsorption performance was achieved across a broad pH range of 3 to 11 and in the presence of substantial amounts of co-existing ions/substances (Cl^-, NO_3^-, SO_4^{2-}, HCO_3^-, and humic acid at concentrations 20–50 times that of the PO_4^{3-}-P concentration). After five adsorption-regeneration cycles, 79 % adsorption capacity remained with material recovery rates >95 % via magnetic separation. A bimetallic synergistic mechanism was revealed via X-ray absorption fine-structure characterizations and density functional theory (DFT) calculations. The electronegativity difference between La and Zn induces interfacial electron redistribution, driving electron back-donation from the La/Zn-O hybridized orbitals to the O 2p anti-bonding orbitals of HPO_4^{2-}, forming stable covalent coordination bonds (La-O-P/Zn-O-P), which allowed the

* Corresponding author.
E-mail address: qiugl@scut.edu.cn (G. Qiu).

https://doi.org/10.1016/j.watres.2025.124753
Received 16 May 2025; Received in revised form 21 September 2025; Accepted 8 October 2025
Available online 9 October 2025

exceptionally high and efficient adsorption of phosphate. This phenomenon is expected to have important implications for the development of novel adsorption materials for advanced removal of phosphate.

1. Introduction

Phosphorus (P) plays an irreplaceable role in cellular energy transfer and the synthesis of genetic materials (Elser, 2012; Yang et al., 2024). However, its excessive discharge into water systems causes severe eutrophication, even at trace concentrations (>0.01 mg P/L) (Li et al., 2025a). Addressing this challenge requires advanced phosphate removal technologies to meet the ultra-low effluent standards (≤0.02 mg P/L). Adsorption is a reliable and promising method for the selective removal of pollutants such as phosphate at low concentrations (Altaf et al., 2023).

The theoretical basis of phosphate adsorption lies in the electron transfer mechanism dominated by Lewis's acid-base interactions. As a hard Lewis base, phosphate preferentially coordinates with hard acid metal ions (Ca^{2+}, La^{3+}, Zn^{2+}) through orbital hybridization to form stable inner-sphere complexes (Beer and Gale, 2001), among which, La^{3+} exhibited exceptional affinity (pK_a=26.16) by readily donating electrons from its 4f orbitals to the non-bonding orbitals of phosphate (Zhang et al., 2022). For example, the commercial adsorbent Phoslock® (La^{3+}-modified bentonite) has been widely applied in global water ecological restoration projects (Spears et al., 2013). However, the high cost of the rare earth metal La limited its larger-scale application. To address this, researchers have developed bimetallic and polymetallic materials by doping metals such as Ca, Mg, and Fe to reduce the use of La. Examples include La-Ca modified bentonite-chitosan hydrogel beads with a phosphate adsorption capacity of 123 mg P/g and La-Fe modified sawdust biochar achieving nearly 100 % phosphate removal at PO_4^{3-}-P concentrations <1.0 mg/L (W. Wang et al., 2024; Yi et al., 2024). Bimetals may modify the electronic structure of the adsorbent, enhance interactions with target ions, and reduce adsorption barriers, thus increasing adsorption capacity and stability (Kong et al., 2024). Whereas, the governing mechanisms are largely unclear in details, limiting the advanced development of bimetallic adsorption materials.

The adsorption of oxyanions is primarily regulated by the orbital interactions between the adsorbate and the metal-oxygen (M-O) sites on the material surface. Enhancing the interfacial electronic cloud density via introducing highly electron-donating elements would potentially enhance the covalency of M-O bonds, thus their interaction with adsorbates. Recently, studies in the area of electrocatalytic water splitting showed that combining 3d metal hydroxides (e.g., NiFe-LDH) with 5d high-valence metals (e.g., W, Cr) can trigger significant 3d-2p-5d orbital hybridization effects, thereby optimizing interfacial charge transfer kinetics and reducing reaction energy barriers (He et al., 2021; Wu et al., 2020; Yang et al., 2018), benefiting the adsorption of intermediates. Notably, however, these studies focused on modulating the adsorption of hydroxyl-oxygen intermediates (e.g., *OOH, *OH) during the oxygen evolution reaction (OER)(Zhai et al., 2021). In contrast, this study employs analogous orbital hybridization mechanisms to enhance the selective capture capability of phosphate in aquatic systems.

Previous studies on bimetallic systems (e.g., La/Fe and La/Zr) showed that for La/Fe (hydr) oxides the oxidation-state shift of Fe were arose solely from Fe-O-P bond formation (Chen et al., 2023; Cui et al., 2023; Sun et al., 2022). Conversely, Kong et al. observed positive shifts of both La 3d and Zr 3d after phosphate adsorption, implying possible La → Zr electron transfer and redistribution, a phenomenon deserves further investigation and understand. Nevertheless, the La/Zr system showed an PO_4^{3-}-P adsorption capacity of 116.2 mg/g which reduced by 25 % after four cycles (Yu et al., 2025), showing rooms for further improvements. In view of its lower electronegativity, Lewis acidity, fixed valence and potential economic advantage, we hypothesize that Zn might be a better company metal with La to form a novel bimetallic system.

The d-orbital hybridization between Zn^{2+} (with filled $3d^{10}$ orbitals) and La^{3+} (with vacant $5d^0$ orbitals) would facilitate the formation of highly covalent M-O bonds, which are expected to significantly improve the redistribution of charge density at the interface, thereby enhancing the electron-capturing ability for oxygen atoms in PO_4^{3-}. This charge transfer mechanism may be further amplified by the electron-donating nature of Zn^{2+}, which would induce a redistribution of local charge density around La^{3+} sites, effectively activating adjacent lattice oxygen species and optimizing their reactivity. Meanwhile, the hard Lewis acid character of La^{3+} drives preferential coordination with the lone-pair electrons of phosphate oxygen atoms, while Zn^{2+} acts as an auxiliary site to modulate the electron-accepting capacity of La^{3+} through acid-base synergistic effects. The adsorption performance of phosphate can be significantly enhanced through a multi-mechanistic coupling process based on electronic and coordination chemistry.

Additionally, despite the surge of bimetallic phosphate adsorbents in recent years (Table S1, Fig. S1), it remains challenging to simultaneously fulfill the following criteria—high capacity, wide pH tolerance, high regeneration retention—within a single material. Systems such as La_1Al_3-BTC, Ce/FcDA/FA-MOF, and MZLCO-45 exhibited appreciable adsorption capacities, yet suffered a 25–49 % capacity loss after 4–5 regeneration cycles (Zhu et al., 2024a; Gao et al., 2024; Liu et al., 2022). Novel material needs to be developed to fulfill the combined requirements for applications.

To verify the hypothesis of electron transfer and overcome the application bottleneck of traditional lanthanum-based and/or bimetallic materials, we designed a novel core-shell structured magnetic mesoporous silica Zn/La bimetallic composite (Zn/La-MMS). This material achieved performance breakthroughs through a triple-synergistic mechanism: 1) Zn^{2+} modulates the electronic structure of La^{3+} through d-orbital coupling, with density functional theory (DFT) calculation confirming its enhanced electron-accepting ability; 2) The Fe_3O_4@SiO_2 core-shell structure enables magnetic separation while the silica matrix suppresses iron leaching; 3) Mesoporous channels maximize the accessibility of active sites.

The resultant adsorbent exhibited not only a significantly higher phosphate adsorption capacity but also a wider applicable pH range (3 to 11). The effects of solution pH and coexisting ions on phosphate adsorption performance were systematically examined. Promising reusability of the material was demonstrated via repetitive adsorption-regeneration tests. The phosphate adsorption mechanisms were further elucidated via comprehensive characterization of the adsorbent's structure, surface morphology, specific surface area (BET), pore size distribution, zeta potential, surface functional groups (XPS/FTIR), crystal structure (XRD), and synchrotron-based X-ray absorption spectroscopy (XAS), combined with density functional theory (DFT) calculations and Bader charge analysis. The results reported in this study are expected to benefit the development of highly effective, readily recoverable, and reusable adsorbents for efficient and reliable removal of phosphate from water and wastewaters.

2. Material and methods

2.1. Chemicals

All chemicals utilized in this study were of analytical grade. Deionized water (DI) (18.2MΩ) was used to prepare all reagents. More details are provided in the Supplementary Material Text S1. Phosphate stock solution was prepared by dissolving 2.197 g of KH_2PO_4 (≥99 %) in 1000 mL of ultrapure water and stored at 4 °C before use. 0.1 M HCl and

NaOH solutions were used for solution pH adjustments.

2.2. Synthesis of materials

A detailed description of the procedures used to prepare the pure Fe_3O_4, the Fe_3O_4@SiO_2, and the Fe_3O_4@SiO_2@mSiO_2 (abbreviated as MMS) can be found in the Supplementary Material Text S2. The protocol for the synthesis of Zn/La doped Fe_3O_4@SiO_2@mSiO_2 composites are as follows: A mixture of 0.2 g of MMS, $ZnCl_2$, and $La(NO_3)_3{\cdot}6H_2O$ each was uniformly mixed using sonication in a solvent mixture consisting of 40 mL of ethanol and 40 mL of DI water for 30 min. Subsequently, the mixture was stirred at 25 °C and 300 rpm. 0.1 M NaOH was gradually added to the mixture until the pH reached 10±0.5. The resultant suspension was then stirred at 25 °C for 4 h (Chen et al., 2019a). The final products were collected via magnetic separation, washed alternately with deionized water and ethanol several times, and dried under vacuum overnight to obtain the Zn/La-MMS composites.

In this study, three Zn^{2+}/La^{3+} molar ratios (i.e., 1:1, 1:2, and 2:1) were investigated. The resulting composites were denoted as Zn/La-x MMS, where "x" represented the molar ratio of Zn^{2+} to La^{3+} (i.e., Zn/La-1, Zn/La-0.5, and Zn/La-2 MMS).

2.3. Characterization

The microstructural morphology and surface elemental distribution of the Zn/La-MMS composites were characterized by scanning electron microscopy (SEM) coupled with energy-dispersive X-ray spectroscopy (EDS). The internal structure and particle size were analyzed using transmission electron microscopy (TEM). X-ray diffraction (XRD) was employed to identify the primary crystalline phases and lattice parameters of Zn/La- MMS composites. Synchrotron X-ray absorption spectroscopy (XAS) was further employed to resolve the local coordination environments and electronic structures of Zn and La. Surface elemental composition and the evolution of binding states of specific elements before and after phosphate adsorption were investigated via X-ray photoelectron spectroscopy (XPS). Fourier-transform infrared spectroscopy (FTIR) was utilized to monitor changes in surface functional groups during the adsorption process. The specific surface area, pore volume, and pore size distribution were determined via nitrogen adsorption-desorption isotherms and calculated based on the Brunauer-Emmett-Teller (BET) model. The magnetization of the samples was measured using a Vibrating Sample Magnetometer (VSM). The electrostatic interaction mechanism (attraction or repulsion) between the material and phosphate was evaluated by measuring the point of zero charge (PZC) through zeta potential analysis before and after adsorption. To assess material stability under varying pH conditions, the leaching concentrations of metal elements were quantified by inductively coupled plasma optical emission spectrometry (ICP-OES). More details of the methods are described in the Supplementary Material Text S3.

2.4. Batch adsorption experiments

To investigate the maximum adsorption capacity and adsorption characteristics of Zn/La-x MMS composite materials, adsorption isotherm experiments were conducted. Phosphate solutions with initial PO_4^{3-}-P concentrations ranging from 3 to 30 mg/L were prepared, and the pH was adjusted to 6.5 (within the typical pH range (6–8) for application, a slightly acidic environment was favorable for adsorption by using the material developed in this study). 10 mg of adsorbent was introduced into a 50 mL phosphate solution. The experiments were carried out at three different temperatures (25, 35, and 45 °C) on a magnetic stirrer at 260 rpm. Samples were collected at 0 min and 24 h, filtered through a 0.22 μm cellulose membrane filter. The remaining PO_4^{3-}-P in the solution was determined using a UV–visible spectrophotometer (UV-6300, Shanghai Jinpeng Analytical Instruments Co., Ltd.). Each sample was measured three times. The detailed calculations for adsorption capacity and removal efficiency can be found in the Supplementary Material Text S4. Adsorption kinetics, pH, and co-existing ions effect experiments were performed following the protocol, with the difference in the kinetics experiment being conducted at a constant temperature of 25 °C. Samples were taken at various time intervals (2, 5, 10, 15, 20, 30, 40, 60, 120, and 240 min) for PO_4^{3-}-P concentration measurement. The pH effect experiment was carried out at pH values of 3, 5, 7, 9, and 11, respectively. In the co-existing ions experiment, different concentrations (200, 500, and 1000 mg/L) of SO_4^{2-}, Cl^-, NO_3^-, and HCO_3^- as well as natural organic matter humic acid (HA), were introduced into the phosphate solution to test their effects on phosphate adsorption. Supplementary information Text S4 provided a detailed description of the adsorption isotherm and adsorption kinetics fitting models.

2.5. Desorption of phosphate and regeneration of adsorbent

To verify the reusability of the Zn/La MMS composite, different concentrations of NaOH solution were used to regenerate the Zn/La MMS after adsorption. The initial PO_4^{3-}-P concentration was 50 mg/L, and the dosage of the adsorbent was 0.5 g/L. Both the adsorption and regeneration/desorption times were 12 h. After optimization, a 1 M NaOH solution was chosen as the regeneration solution. After the first round of phosphate adsorption, the Zn/La MMS composite material was separated using an external magnetic field, washed several times with pure water, and air-dried. The volume of the regeneration solution was determined based on a mass/volume ratio of 1 g/L. Desorption was carried out at 25 °C and 260 rpm. To evaluate the reusability of the used adsorbent, a total of five consecutive cycles of adsorption and regeneration were conducted. The regeneration efficiency was assessed by measuring the recovery of phosphate adsorption capacity after regeneration.

2.6. Application in real wastewater

To explore the potential of Zn/La MMS composites in real water and wastewater treatment, three different types of water sources (tap water, landscape lake water, and secondary effluent from a wastewater treatment plant) were tested. Tap water was sourced from the laboratory's water supply system. Landscape lake water was collected in the campus of the South China University of Technology in Guangzhou. The secondary effluent was obtained from the end of an aerobic treatment tank of a wastewater treatment plant in Guangzhou. After filtering via 0.22 μm cellulose filters, the PO_4^{3-}-P concentration was uniformly adjusted to 3.0 mg/L. Zn/La MMS composites were dosed at 0.2 g/L. Water samples were collected at fixed time intervals for the measurement of PO_4^{3-}-P concentrations. Besides, 2 L of water was collected from a typical eutrophic water body in South China, immediately filtered through a 0.22 μm membrane, and stored at 4 °C. Zn/La-0.5 MMS (0.1 g) was added, and the suspension was shaken at 150 rpm and 25 °C for 6 h.

In addition, column experiments were conducted. 2 g of vacuum-dried Zn/La-MMS were packed into a 10 mm × 200 mm glass column (the bed height was 25 mm; the empty-bed volume was 2.0 mL). Porous baffle at both ends prevented material loss. The column was operated in up-flow mode at 25 °C using a peristaltic pump (Longer BT100–1 L). The superficial velocity was 2.5 m/h, resulting in an EBCT of 5 min. The influent PO_4^{3-}-P concentration was 0.083 mg/L. Every 20 mL of effluent was filtered (0.45 μm) and analyzed for PO_4^{3-}-P, Zn and La concentration.

To evaluate the mechanical stability of Zn/La-MMS under hydraulic shear, a laboratory-scale wet-abrasion test was conducted. 200.0 ± 0.5 mg sample, which was dried at 60 °C for 12 h under vacuum, was placed on a magnetic stirrer with 200 mL de-ionized water (25 °C, pH=7.0 ± 0.2),resulting in a solid/liquid ratio of 1 g/L. A magnetic stirrer plate provided uniform shear at 600 rpm for 2 h. Immediately after shearing, the suspension was filtered through a 0.45 μm membrane and rinsed

with 50 mL deionized water to remove loosely attached fines. The retained cake was vacuum-dried at 60 °C to constant mass. The mass loss was calculated using Eq. (1):

$$Mass\ loss(wt\%) = \frac{m_0 - m_t}{m_0} \times 100\% \quad (1)$$

Where m_0 is the initial dry mass and m_t is the dry mass after shearing.

2.7. DFT calculation

In this study, first-principles calculations based on density functional theory (DFT) were performed using the Vienna Ab-initio Simulation Package (VASP) to explore the adsorption mechanisms of the materials (Kresse and Furthmüller, 1996; Surendranath et al., 2010). The projector augmented wave (PAW) pseudopotential was employed to describe the interactions between the ionic cores and valence electrons. The Perdew-Burke-Ernzerhof (PBE) functional was used to treat the exchange-correlation energy (Perdew et al., 1996). During the structural optimization, the cutoff energy of the plane-wave basis set was 450 eV. The energy convergence threshold for electronic self-consistent iterations was 10^{-5} eV. The atomic positions were fully relaxed using the conjugate gradient algorithm until the residual forces on all atoms were <0.02 eV·Å^{-1}.

The adsorption energy (Ead) of phosphate was calculated using Eq. (2):

$$E_{ad} = E_{surf/anion} - E_{surf} - E_{anion} \quad (2)$$

Where $E_{surf/anion}$ is the total energy of the complex after adsorption; E_{surf} is the ground-state energy (0 K) of the adsorbent; $E_{anion}$is the ground-state energy of phosphate.

The electron density distribution obtained from DFT calculations was partitioned and assigned to individual atoms (Sanville et al., 2007). By comparing the charge variations before and after adsorption, the charge transfer between the surface and the adsorbate was elucidated. A negative net charge on an atomic site indicates that the atom acts as an electron acceptor during the adsorption process.

In addition, Bader charge analysis was employed to quantitatively characterize the charge distribution between the adsorbate (phosphate) and the adsorbent surface, quantifying the electron transfer accompanying coordination-bond formation and providing quantitative evidences for the hypothesis of d–π* back-donation from the La/Zn d orbitals to the O 2p* antibonding orbitals.

3. Results and discussion

3.1. Characterization of zn/la MMS composites

3.1.1. SEM

The preparation procedure of the Zn/La-x MMS composites was illustrated in Fig. 1a. Fig. 1b and 1c showed the SEM images of the MMS and Zn/La-x MMS, respectively. Fig. 1d was the TEM image of the MMS. The MMS sample had a smooth spherical shape with open pores (ranging from 300 to 350 nm) on its surface. After loading with metal (Zn and La) hydroxides, the shape of the MMS remained unchanged, with increased particle size and good dispersibility. However, the surface of the spheres became rougher, and the open pore channels became no longer distinctly visible on the surface (Fig. 1c). Fig. 1d illustrated the ferric tetroxide particles, which were spherical particles sized between 200 and 300 nm, encapsulated with a layer of silicon dioxide shell to form the Fe_3O_4@SiO_2 structure, with the shell being about 20–25 nm thick to prevent the oxidation of Fe_3O_4. Outside this protective layer, an additional layer of dendritic mesoporous silicon dioxide (Fe_3O_4@SiO_2@mSiO_2) was coated, which was about 25–30 nm thick, designed to increase the specific surface area of the adsorbent and provide a mesoporous structure to accommodate metal hydroxides.

3.1.2. BET

Table S2 displayed the specific surface area (S_{BET}), pore volume, and average pore size of all samples. The N_2 adsorption-desorption isothermal curves and pore size distribution curves of MMS and Zn/La-x MMS were shown in Fig. 2. MMS showed a type-IV isothermal curve. After Zn and La loading, the type of the curve was unchanged, indicating the retention of mesoporous structures. As shown in Table S2, the pristine MMS exhibited a high specific surface area and pore volume (332.70 m^2/g and 0.78 cm^3/g, respectively). However, these values decreased significantly in all Zn/La-x MMS composites, with the extent of reduction depending on the Zn/La ratio. The decrease was much more pronounced with the increase in Zn contents, attributing to the formation of $Zn(OH)_2$/$La(OH)_3$ during metal loading. However, the average pore size of Zn/La-x MMS increased compared to MMS. The pore size distribution of Zn/La-x MMS displayed spikes centered between 10–15 and 50–70 nm, suggesting that the ordered mesoporous structure was maintained after Zn/La loading. The spikes at 50–70 nm may be due to the filling of internal voids and the formation of macropores by Zn $(OH)_2$/La $(OH)_3$ stacking on the SiO_2 mesoporous shell.

3.1.3. Vibrating sample magnetometer (VSM) analysis

The magnetic properties of Fe_3O_4, MMS, and Zn/La-0.5 MMS were characterized at room temperature using a vibrating sample

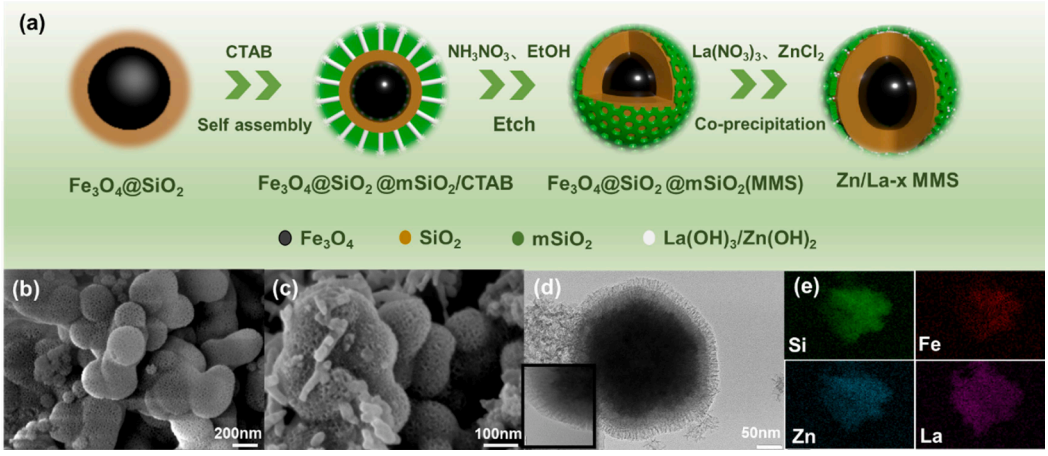

Fig. 1. (a) Preparation of Zn/La-loaded Fe_3O_4@SiO_2@mSiO_2(Zn/La-x MMS); SEM images of (b) MMS and (c) Zn/La-x MMS; (d) TEM images of MMS and (e) elemental mapping images of Zn/La-x MMS.

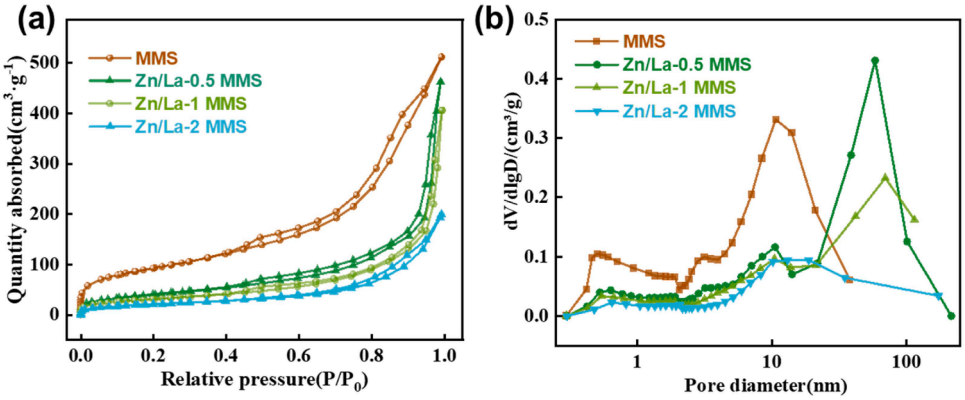

Fig. 2. (a) N_2 adsorption-desorption isotherm curves, (b) pore size distribution curves.

magnetometer (VSM) (Fig. S2). Results show that both materials exhibit superparamagnetic behavior. The saturation magnetization (Ms) of MMS is as high as 60.5 emu/g. Although the Ms values of MMS and Zn/La-0.5 MMS, after being coated with SiO_2/mSiO_2 shells, are reduced to 3.03 and 2.69 emu/g, respectively, due to the magnetic core shielding effect, rapid solid-liquid separation was still effectively achieved through an external magnetic field (Fig.S2), confirming its operability in practical applications.

3.2. Adsorption performance

3.2.1. Adsorption kinetics

The adsorption kinetics of Zn/La-x MMS composites were investigated at a dosage of 0.2 g/L and an initial PO_4^{3-}-P concentration of 10 mg/L at a pH value of 6.5. The results were depicted in Fig. 3a-c. The adsorption rate of the Zn/La-x MMS composites surged within the first 20 min. This rapid adsorption was attributed to the large specific surface area and pore size structure, which facilitated the rapid diffusion of PO_4^{3-} into the Zn/La-x MMS composites and their interaction with the active sites. Subsequently, equilibrium was reached. To further elucidate the adsorption mechanisms of Zn/La-x MMS, the experimental data were fitted to pseudo-first-order (Yuh-Shan, 2004), pseudo-second-order (Ho, 2006), and intra-particle diffusion models (Furusawa and Smith, 1974). The fitting results and parameters were presented in Fig. 3a-c and Table S3. Notably, the correlation coefficients obtained from the pseudo-second-order fitting for Zn/La-0.5 MMS, Zn/La-1 MMS, and Zn/La-2 MMS were 0.997, 0.998, and 0.998, respectively, which were superior to those obtained from the pseudo-first-order kinetic model (0.993, 0.996, and 0.997, respectively). These findings suggested that the phosphate adsorption behavior of Zn/La-x MMS was more consistent with the pseudo-second-order kinetic model, implying that the adsorption was primarily governed by chemisorption, involving the sharing and/or transferring of electrons (Chang et al., 2021). While the pseudo-second-order kinetic model effectively characterized phosphate adsorption, the diffusion mechanism required further elucidation through the application of an intra-particle diffusion model. Therefore, experiments were conducted at different PO_4^{3-}-P concentrations (10, 20 and 30 mg/L). The adsorption process may be divided into three stages, indicating the influences of multiple steps. The relevant parameters and R^2 values for the intra-particle diffusion model fit were summarized in the Table S4. The first stage (0–30 min) corresponded to liquid membrane diffusion, primarily involving the transport of phosphate from the solution to the adsorbent surface. The steep slopes during this stage suggested that the process was driven by the high initial phosphate concentration. The second stage (30–100 min) represented intra-particle diffusion, where phosphate was transported from the adsorbent surface

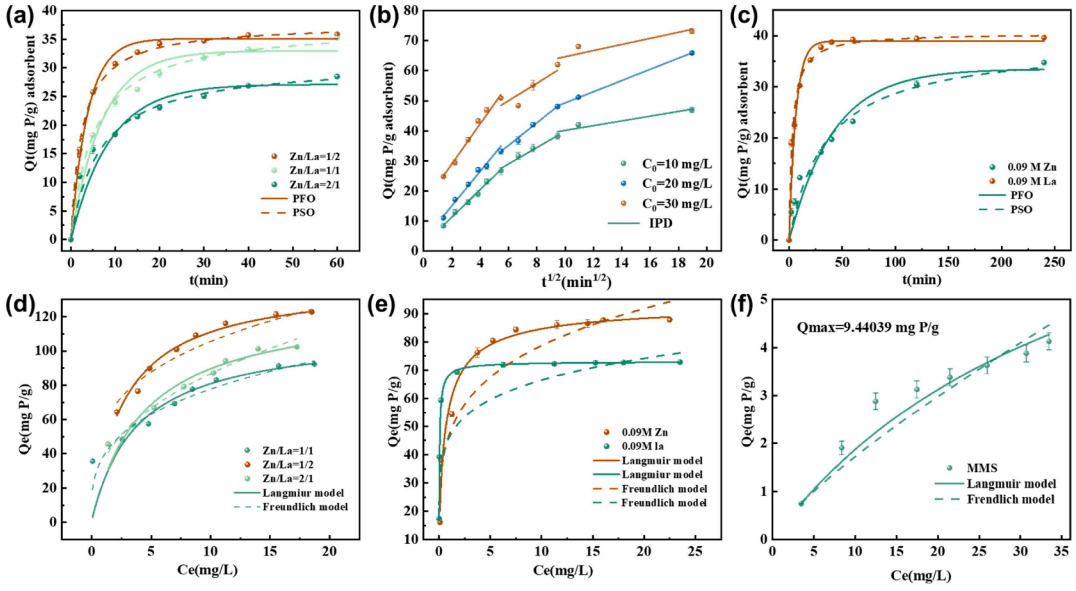

Fig. 3. Kinetic model fitting for the P-adsorption by Zn/La-x MMS, using (a) PFO, PSO, and (b) IPD models; (c) PFO, PSO model fitting for the P-adsorption by Zn/La MMS; Adsorption isotherms for phosphate by (d) Zn/La-x MMS; (e) Zn/La MMS; (f) MMS.

to its internal pore structure. The third stage (100–360 min) corresponded to the equilibrium phase, characterized by a smaller slope due to the decreased phosphate concentration in the solution and the slowed intra-particle diffusion rate. Notably, none of the linear segments passed through the origin, indicating that although intra-particle diffusion influenced the phosphate adsorption behavior and rate of Zn/La-x MMS, it was not the dominant process (Zhang et al., 2022).

3.2.2. Adsorption isotherms

Isothermal adsorption experiments were carried out to investigate the type of adsorption and the maximum adsorption capacity of Zn/La-x MMS. Adsorption results were collected within an initial PO_4^{3-}-P concentrations range of 3–30 mg/L. The data were fitted using Langmuir and Freundlich models. As shown in Fig. 3d-e, the adsorption capacity increased with increased equilibrium concentrations. The adsorption capacity of MMS was 9.44 mg P/g, which for Zn/La alone was 94.42 and 73.18 mg P/g, respectively, attributing to the fact that the K_{sp} of $Zn_3(PO_4)_2$ was higher than $LaPO_4$. The adsorption capacity of Zn/La-x MMS was the highest as compared to Zn/La and MMS alone. Table S5 lists the results of the parameters derived from Langmuir and Freundlich model fitting. Langmuir was able to better fit the experimental data ($R^2 > 0.97$), indicating that the adsorption of phosphate by Zn/La-x MMS was dominated by a monolayer homogeneous adsorption. The maximum adsorption capacities for Zn/La-1 MMS, Zn/La-0.5 MMS, and Zn/La-2 MMS were 11.36, 140.91, and 128.72 mg P/g, respectively, which were significantly higher than those of previously reported similar adsorbents (Table S6).

The molar ratio of phosphorus to total metals (Zn+La), denoted as P/M, is frequently employed to indicate the utilization efficiency of active sites in metal-based adsorbents (Zhang et al., 2017). Literature results showed that the P/M values of La-containing adsorbents is typically below 1.13 after adsorption (Zhu et al., 2024a). ICP-OES analysis of the Zn/La-MMS showed that it contains 2.91 wt % Zn and 11.19 wt % La, corresponding to a P/M of 1.76 after adsorption, implying that more active sites were exposed and participated in phosphate binding in the Zn/La-MMS (Table S11).

3.2.3. Adsorption thermodynamics

Fig. 4c and Table S7 presented the thermodynamic parameters for the adsorption of phosphate by Zn/La-0.5 MMS (for detailed calculation methods, see Text S4). The entropy change (ΔS) and enthalpy change (ΔH)) values were determined using a linear regression model. The ΔH value for Zn/La-0.5 MMS was 14.54 kJ/mol, and the ΔS value was 64.02 KJ/mol·K^{-1}, indicating that the adsorption of phosphate by Zn/La-0.5 MMS was an endothermic process (Peng et al., 2019). Furthermore, the Gibbs free energy (ΔG) ranged from −5.85 to −4.56 kJ/mol, which was negative, and slightly increased at rising temperatures, indicating that the adsorption reaction was spontaneous and consistent with the phenomenon that the adsorption capacity increased with temperature (Zhang et al., 2022).

3.2.4. Effects of pH and coexisting ions

Based on the experimental data, the Zn/La-0.5 MMS composite demonstrated outstanding phosphorus removal performances in both adsorption kinetics and adsorption isotherms, making it an optimal material for further analysis. pH value is a key factor influencing phosphate adsorption. As shown in the Fig. 4a. under acidic and neutral conditions, the Zn/La-0.5 MMS composite exhibited excellent phosphate removal performance, which decreased with the increase in pH values. At pH = 3, with an initial PO_4^{3-}-P concentration of 11 mg/L, the adsorption capacity reached 54.25 mg P/g, which decreased to 29.25 mg P/g as the pH value increased to 11, with a reduction of 46.09 %. It was evident that the phosphate adsorption capacity of Zn/La-0.5 MMS was largely determined by the solution pH. This could be attributed to several aspects: Firstly, the surface charge of the adsorbent played a crucial role (Mahmoud et al., 2024). As shown in Fig. 4b, the point of zero charge (pH_{pzc}) of the Zn/La-0.5 MMS was 7.78, which decreased to 6.3 after the adsorption of phosphate. When the solution pH was below 7.78, the hydroxyl groups on the surface of the adsorbent became protonated and positively charged, which promoted the electrostatic attraction of the negatively charged $H_2PO_4^-$ and HPO_4^{2-} in the aqueous solution, enhancing phosphate adsorption (Elkhlifi et al., 2022), Conversely, when the solution pH was above 7.78, the hydroxyl groups on the surface of the adsorbent were deprotonated and negatively charged. The higher pH, the stronger negative charged, and the more likely there was electrostatic repulsion against phosphate, thereby reducing the phosphate adsorption capacity (Yin et al., 2022). Another aspect affecting the adsorption was the different forms of phosphate

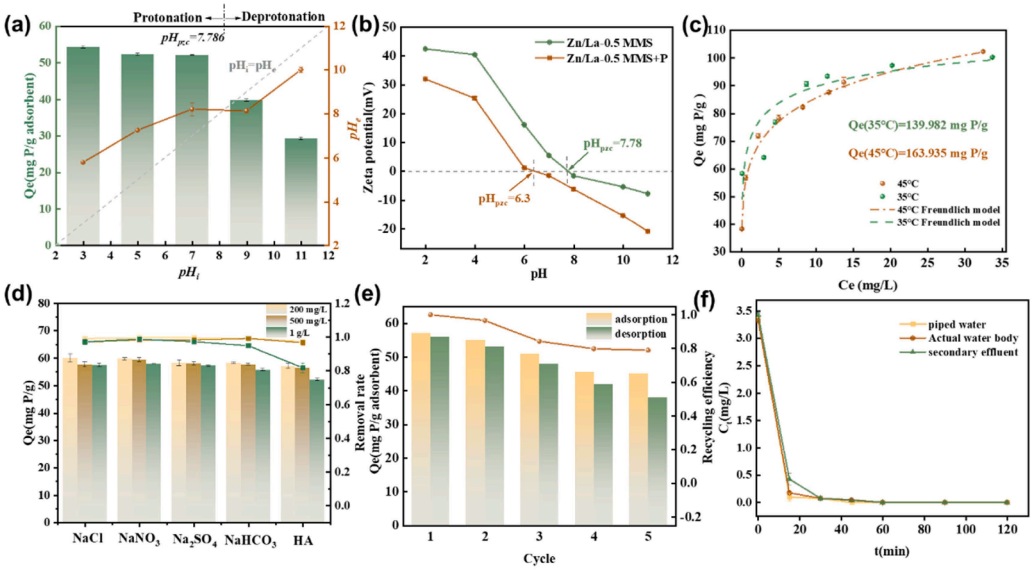

Fig. 4. (a) The P-adsorption capacities of Zn/La-0.5 MMS at different pH; (b) The pH_{pzc} of Zn/La-0.5 MMS before and after adsorption; (c) Adsorption isotherms fitting for P adsorption by Zn/La-0.5 MMS under 308 K and 318 K (C_0=3.0–50.0 mg/L, pH=6.5, T = 308 K and 318 K); (d) The interference of coexisting anions on P-adsorption (C_0=11 mg/L, pH=6.5, T = 298 K); (e) Adsorption and desorption cycles performance of Zn/La-0.5 MMS (C_0=11 mg/L, pH=6.5, T = 298 K); (f) Phosphate removal from synthetic wastewater.

present under different pH conditions: at pH < 2.0, H_3PO_4 is the predominant phosphate species. Within the pH ranging of 2.13–7.20, $H_2PO_4^-$ was the primary form. At pH 7.20–12.13, HPO_4^{2-} predominated (Chang et al., 2021). Additionally, under alkaline conditions, a large amount of OH^- in the solution competed with phosphate for active adsorption sites on the surface of the adsorbent, leading to decreased phosphate adsorption. The pH of the solution increased after adsorption, mainly owing to the ligand exchange between phosphate and hydroxyl groups on the surface of the adsorbent, resulting in the release of OH^- into the solution and thus increased pH values (Kong et al., 2024). To assess the stability of the Zn/La-0.5 MMS under different pH conditions, the leaching of Zn and La was examined under different pH conditions (3.0–11.0). As shown in Fig. S3, generally higher concentration of Zn and La ions were detected under acidic conditions, indicating relatively low stability at acidic environments. As the solution pH increased to 7 and above, the leaching of those metal ions became negligible, with concentration levels stabilized at about 0.18 and 0.23 mg/L for Zn and La, respectively. Considering that the pH conditions in water and wastewater were typically between 6–9, the Zn/La-0.5 MMS desirable stability in real applications.

High concentrations of anions in water could affect the adsorption of phosphates. Commonly found anions in wastewater include Cl^-, NO_3^-, SO_4^{2-}, and HCO_3^-. Additionally, natural organic matter such as humic acid (HA) might also compete with phosphates for active adsorption sites, thereby having the potential to reduce the phosphate adsorption efficiency. Therefore, this study analyzed the effects of these coexisting anions/organic matter at different concentrations (200, 500, and 1000 mg/L) on the adsorption of phosphates. As shown in Fig. 4d, Cl^-, NO_3^-, SO_4^{2-} had little effect on the adsorption of phosphates. HCO_3^- and HA had limited interference with phosphate adsorption at concentrations below 200 mg/L. However, at concentrations above 500 mg/L, their interfering effects started to show up, leading to decreased phosphate adsorption capacity. Whereas, at any cases the reduction of the phosphate adsorption capacity was below 20 %. At low HA concentrations, Zn-La-0.5 MMS possessed a multitude of adsorptive sites for the adsorption of phosphate and HA. Yet, at increased HA concentrations, La was more inclined to bind with HA to form La-HA colloidal complexes, which in turn diminished the adsorption capacity of the adsorbents (Kong et al., 2024) (although it is typically less likely that the HA concentration may pass 200 mg/L in real water or wastewater samples). For HCO_3^-, its presence could elevate the solution pH. Given that the solubility product constant (K_{sp}) of $La_2(CO_3)_3$ was (3.98×10^{-34}) comparable to that of $LaPO_4$ (3.7×10^{-23}), the competition of HCO_3^- with phosphates is expected but only at high HCO_3^- concentrations (Li et al., 2025a).

3.2.5. Real water/wastewater applications

Real water/wastewater tends to have more complex compositions and more influencing factors on phosphate adsorption, so it is necessary to use real water/wastewater to evaluate the adsorption performances of Zn/La-0.5 MMS. Tap water, landscape lake water and secondary effluent from a local WWTP (with their origin PO_4^{3-}-P concentrations of 0.00, 0.02 and 0.17 mg/L, respectively) were used to formulate phosphate solutions with an initial concentration of 3.0 mg/L to investigate the adsorption performances of Zn/La-0.5 MMS for applying to real water/wastewater with low phosphate concentrations. As shown in Fig. 4f, the Zn/La-0.5 MMS were able to rapidly reduce the PO_4^{3-}-P concentration to 0.02 mg/L within 20 min, indicating the promising applicability of Zn/La-0.5 MMS for real applications.

To understand of the performance of Zn/La-0.5 MMS under field application conditions, 0.1 g of the composite was added in 500 mL surface water collected from a river nearby the Pearl River in Guangzhou. The total phosphorus (TP) concentration in the surface water sample is 0.10 mg/L, exceeding the Class III limit of the Chinese Surface Water Standard (0.05 mg P/L). Co-existing anions were also abundant, with SO_4^{2-}, NO_3^- and HCO_3^- concentrations of 27.2, 0.74 and 85.5 mg/L, respectively (Table S8). After adsorption, the residual TP was reduced to 0.013 mg/L, achieving an 86 % removal, demonstrating the applicability of Zn/La-0.5 MMS in real water samples with complex compositions.

3.2.6. Regeneration and reuse of zn/la-0.5mms

For ideal phosphate adsorbents, in addition to the excellent phosphate adsorption capabilities, their recyclability was also an important indicator for assessing their economic viability. The effects of NaOH concentrations on the desorption efficiency were investigated, with specific experimental results shown in the Supplementary Material Fig. S4. As the increase in the concentration of NaOH solution, the desorption efficiency increased continuously. The desorption efficiency reached 88.6 % with 1 M NaOH solution. Further increasing the concentration of NaOH only increased the desorption efficiency by 0.67 %. Thus, 1 M NaOH was used as the eluent to evaluate the material's regeneration performance. As shown in Fig. 4e, >78 % desorption capacity (44.99 mg P/g) remained after five cycles. The reason for the decrease in adsorption capacity might be that some active sites were permanently occupied and could not be eluted. Despite the slightly reduced adsorption capacity over time, the regeneration performance of the material is overall desirable.

After four cycles, the XRD pattern of Zn/La-MMS showed almost no noticeable change (Fig. S5). The characteristic magnetite diffraction peaks at (311) and (511) were largely unchanged, confirming the structural stability of the framework after alkaline regeneration. Meanwhile, the disappearance of the $La(OH)_3$ and $Zn(OH)_2$ peaks originally located at 15.6° and 27.9° indicates that the metal sites were successfully regenerated. ICP-MS analysis revealed that the leaching of Zn and La in the regenerant were both below 0.15 mg/L (Table S11), demonstrating the stability and practical safety of Zn/La-MMS (Fig. S5).

To assess the dynamic column performance, we conducted tests at a superficial velocity of 2.5 m/h and an empty-bed contact time (EBCT) of 5 min. With 2 g Zn/La-MMS, at an influent PO_4^{3-}-P concentration of 0.083 mg/L, 1050 bed volumes were achieved with effluent PO_4^{3-}-P concentrations < 0.02 mg/L. Zn and La in the effluent remained below 0.05 and 0.01 mg/L, respectively, demonstrating its long-term stability (Fig. 5). A mini wet-abrasion test showed a mass loss of 0.7±0.1 wt % after 2 h of hydraulic shearing at 600 rpm (Table S14), lower than that (< 1.5 wt %) reported for analogous Fe_3O_4-based granules (Cheng et al., 2024; Thijs et al., 2023). These results demonstrated the sufficient mechanical integrity and practical relevance of the Zn/La-MMS. Additionally, previous pilot-scale studies demonstrated that the adsorbent-magnetic separation process is readily scalable (Drenkova-Tuhtan et al., 2017; Salinas et al., 2018), adding to the applicability of the Zn/La-MMS developed in this study.

3.3. Adsorption mechanism

3.3.1. XRD

X-ray diffraction (XRD) analysis of the crystallinity and structural changes of MMS and Zn/La-0.5 MMS before and after adsorption were shown in Fig. 6a. The raw MMS primarily displayed crystal phases of Fe_3O_4 and SiO_2, with characteristic diffraction peaks of SiO_2 located at 20.8° and 26.6°, corresponding to its (100) and (011) crystal planes, respectively (Mi et al., 2022). By comparing with the Fe_3O_4 standard card [JCPDS#99–000–2246], both MMS and Zn/La-0.5 MMS exhibited distinct diffraction peaks at 29.96°, 35.5°, and 57.04°, corresponding to the (220), (311), and (511) crystal planes, respectively (Chen et al., 2019b). This indicated that the material maintained the cubic spinel structure of Fe_3O_4 before and after the loading of Zn/La, suggesting that the loading of Zn/La did not affect the structure of Fe_3O_4. Furthermore, the newly emerged diffraction peaks after the loading of metals on MMS matched well with the characteristic peaks of La $(OH)_3$ and ZnO, confirming the successful loading of Zn/La onto the MMS. Specifically, these peaks appeared at 15.6°, 27.9°, 39.2°, and 52.4°, corresponding to the

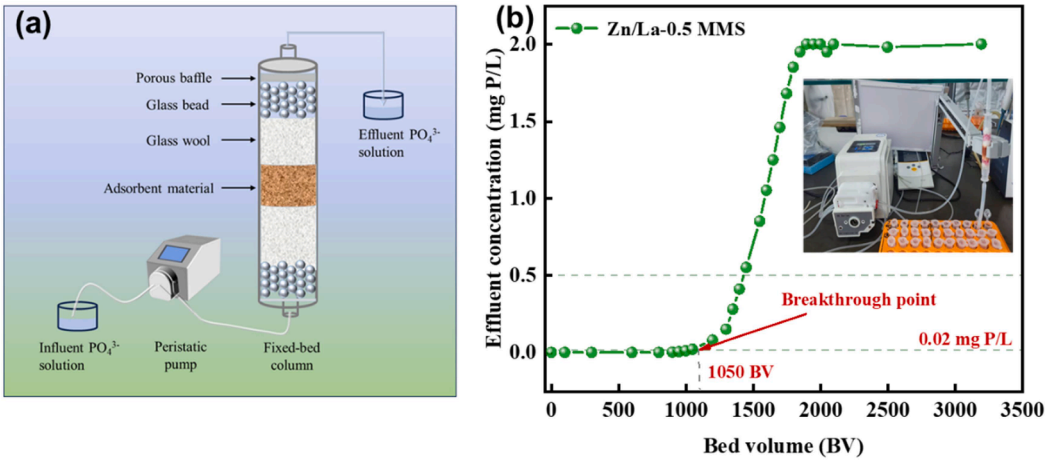

Fig. 5. (a) Schematic illustration of small-scale column experiment; (b) Breakthrough curve in a fixed-bed column experiment. (Initial P concentration: 0.083 mg/L, superficial velocity: 2.5 m/h).

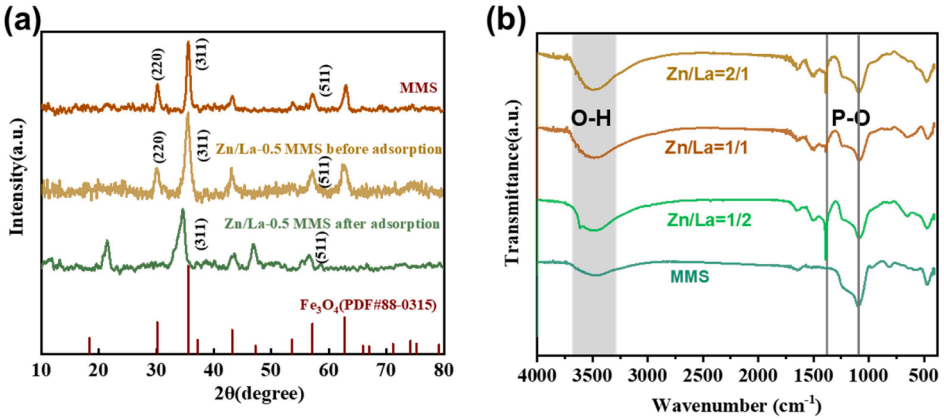

Fig. 6. (a) XRD spectra of MMS and Zn/La-0.5 MMS before and after adsorption, and (b) FTIR spectra of MMS and Zn/La-x MMS after adsorption.

(100), (101), (201), and (211) crystal plane $La(OH)_3$ (JCPDS#83–2034) (Kong et al., 2019), and at 31.05°, 33.1°, 37.58°, and 42.2°, corresponding to the (100), (002), (101), and (220) crystal planes of ZnO (JCPDS#5–0664) (Nakarmi et al., 2020). After phosphate adsorption, the original main diffraction peaks of $La(OH)_3$ in Zn/La-0.5 MMS significantly weakened. A new peak appeared at 48.5°, attributed to the (212) plane of $LaPO_4$, indicating the transformation of $La(OH)_3$ into La-P complexes through inner-sphere complexation (Zhang et al., 2021). Additionally, new peaks observed at 9.7° and 13.4° correspond to the (020) and (220) crystal planes of $Zn_3(PO_4)_2$, respectively (Xia et al., 2024), indicating that ligand exchange occurred between metal hydroxides and phosphates, forming phosphate compounds and contributing to the adsorption and removal of phosphates.

3.3.2. FTIR

Fourier Transform Infrared Spectroscopy (FTIR) was used to analyze the changes in the surface functional groups of MMS and Zn/La-x MMS composite materials before and after the introduction of Zn and La, as well as after the adsorption of phosphate. As shown in Fig. 5b, the FTIR spectra of all adsorbents covered a wavenumber range from 4000 to 500 cm^{-1}. A broad band was observed between 3400 and 3650 cm^{-1}, attributed to the bending vibrations of water molecules (H—O-H) and the stretching vibrations of hydroxyl groups (-OH) (Nguyen et al., 2020). Compared to MMS, the intensity of the peak at 3500 cm^{-1} in the Zn/La-x MMS composites increased, likely due to an increase in the content of hydroxyl groups in La $(OH)_3$, which was also confirmed in the XRD patterns. The peak at 1050 cm^{-1} corresponds to the asymmetric stretching vibrations of Si-O-Si (Wang et al., 2008), while the peak at 795 cm^{-1} corresponds to the bending vibrations of Si-O-H (Li et al., 2016). Additionally, the peaks at 430 and 582 cm^{-1} are attributed to the vibrations of Fe-O bonds in Fe_3O_4 (Li et al., 2025b). The positions and intensities of these peaks did not change significantly before and after metal loading. However, after phosphate adsorption, two new significant peaks (gray solid lines) appeared at 1138 and 1075 cm^{-1} for the Zn/La-x MMS, which were related to the stretching vibrations of P-OH and P-O bonds in phosphate (Song et al., 2019; Wang et al., 2024b), indicating the successful adsorption of phosphate. The peaks at 429 and 1633 cm^{-1} in Zn/La-x MMS were mainly due to the characteristic lattice vibrations of Zn-O and La-OH (Frost et al., 2001; D. D. Li et al., 2025). The weakening of these peaks after P adsorption further confirmed the changes in M-O bonds during the adsorption process, leading to the formation of M-P and M-O-P bonds (where M represented Zn and/or La).

3.3.3. XPS

XPS analysis was performed to further elucidate the adsorption mechanisms. The fine spectra of four elements—O, Zn, La, and P—as well as the whole spectrum analysis before and after phosphate adsorption were displayed in the Fig. 7. All the plots were corrected with the C1s peak (284.80 eV). In Fig. 7a, Zn2p, La3d, O1s, N1s, and C1s were observed. The appearance of a new P2p peak upon adsorption suggested effective adsorption of phosphate. In addition, the standard P2p peak binding energy of KH_2PO_4 was 134.0 eV, which changed to 133.3 eV after adsorption, decreased by 0.7 eV, suggesting the formation of new chemical bonds (M-O-P) in Zn/La-0.5 MMS after phosphate adsorption

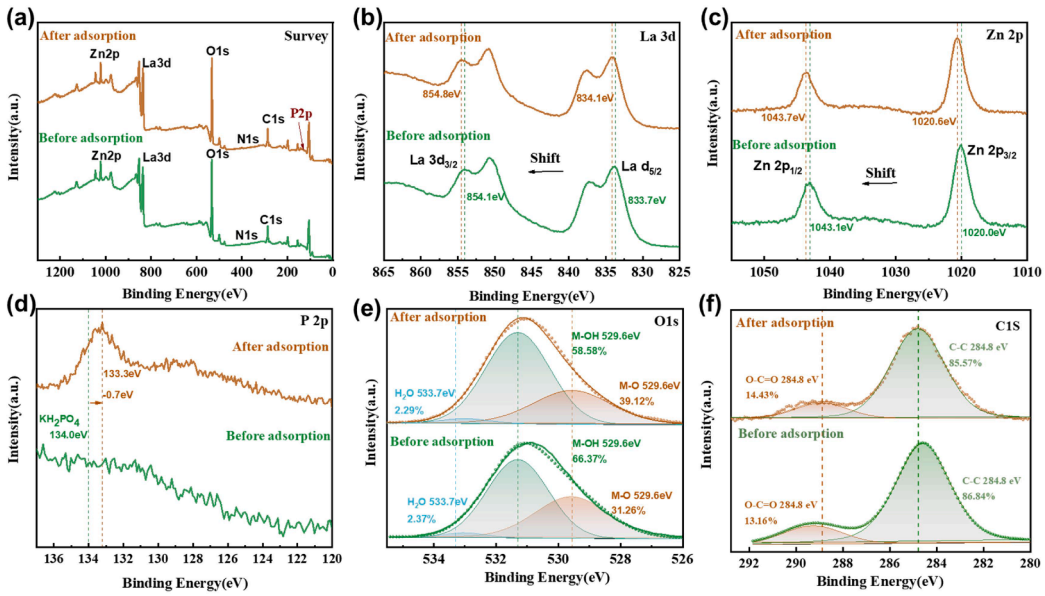

Fig. 7. XPS patterns of Zn/La-0.5 MMS before and after P-adsorption: (a) Survey spectra; (b) La 3d P 2p; (c) Zn 2p; (d) P 2p; (e) O 1 s; (f) C 1 s.

(Liu et al., 2023). The high-resolution spectra of Zn2p and La3d were shown in Fig. 7b and 7c. After adsorption, the positions of these peaks shifted to the left, indication increased binding energies due to the transfer of valence electrons and formation of complex (Yan et al., 2016; Zhang et al., 2022), e.g., the binding energies of the characteristic peaks located in $Zn2p_{1/2}$ and $Zn2p_{3/2}$ increased from 1043.1 to 1020.0 eV to 1043.7 and 1020.6 eV, respectively. Those of the characteristic peaks located in $La3d_{3/2}$ and $La3d_{5/2}$ increased from 854.1 to 833.7 eV to 854.8 and 834.1 eV, respectively. The positive shifts in the binding energies of La 3d and Zn 2p orbitals (Fig. 7b and c) indicated the formation of coordinate bond between metal atoms and phosphate species driven by the aqueous polarization of $H_2PO_4^-$ (Zhu et al., 2024b). According to molecular orbital (MO) theory, this phenomenon arose from two synergistic charge transfer mechanisms: (1) intrinsic charge redistribution due to the electronegativity difference between La and Zn, and (2) directional electron donation from La to Zn mediated by bridging O2p orbitals. These interactions collectively stabilize the $[MO_6]$-PO_4^{3-} coordination structure (Xiang et al., 2019). Consequently, the Zn-La electron coupling not only reinforced phosphate chemisorption through hydrogen bonding but also enhanced overall adsorption capacity via optimized electronic synergy. The high-resolution fine spectrum of O1s was shown in Fig. 7e, and was decomposed into three oxygen-bond peaks at 529.6, 531.3, and 533.7 eV, corresponding to surface lattice oxygen (M-O), surface hydroxyl oxygen (M-O-H), and physically adsorbed water (H_2O), respectively. After adsorption, M-O increased from 31.26 % to 39.12 %, while M-OH decreased from 66.37 % to 58.58 %, suggesting that the adsorption of phosphate may have led to partial substitution of M-OH in the material. Phosphate formed complexes with Zn^{2+}/La^{3+}(Lan et al., 2022). The C1s spectrum can be decomposed into two characteristic peaks: the C—C bond located at 284.8 eV, and the O—C = O bond at 288.9 eV. After phosphate adsorption, the relative intensity of the C—C peak increased from 85.57 % to 86.84 %, which may be due to the formation of more stable C—C bonds on the surface of Zn/La-0.5 MMS during phosphate adsorption. At the same time, the area of the O—C = O peak decreased by 1.27 %, indicating that hydroxyl groups participated in the chemical process accompanying phosphate adsorption (Li et al., 2025a).

3.3.4. *DFT calculation*

To further explore the differences in phosphate adsorption mechanisms among Zn/La-0.5 MMS, Zn MMS, and La MMS, density functional theory (DFT) was employed in this study to simulate the interaction processes between the material surfaces and $H_2PO_4^-$ (Fig. 8a). The geometric optimization of the material structures before and after adsorption, as well as the energy calculation results, indicated that the adsorption energy of Zn/La-0.5 MMS for $H_2PO_4^-$ (Ead = −6.17 eV) was significantly higher than that of the monometallic materials (Zn MMS: −5.03 eV; La MMS: −4.46 eV, see Table S9). This suggested that the bimetallic composite significantly enhanced the driving force for phosphate adsorption. The negative values of Ead confirmed that the adsorption processes of all three materials were energetically spontaneous, and the larger the absolute value of Ead, the stronger the binding strength of the material surface to the target anion. The DFT calculation results were highly consistent with the batch adsorption experimental results, further explaining the mechanisms by which the bimetallic composite material Zn/La-0.5 MMS had superior phosphate adsorption performance compared to the monometallic systems (Zn MMS and La MMS).

To further elucidate the bonding mechanism between phosphate and Zn/La-0.5 MMS, the interfacial electron transfer characteristics were revealed through differential charge density ($\Delta\rho$) and Bader charge analysis. As shown in Fig. 8b, c and d, yellow regions indicated increased electron density on the oxyanions. Blue regions indicated decreased electron density on the doped La/Zn atoms. The HPO_4^{2-} anion gained 0.74e from the material surface (yellow region in $\Delta\rho$), while the coordinated La and Zn atoms lost 2.13e and 1.34e, respectively (blue region). Bader charge analysis confirmed electron transfer from the Zn/La-0.5 MMS surface to oxygen anions during phosphate adsorption. This charge transfer originated from a reverse electron transfer mechanism, where the bimetallic synergistic effect of Zn/La induced electron injection from occupied orbitals of the adsorbent (e.g., La/Zn-O hybridized orbitals) into the unoccupied O 2p antibonding orbitals of HPO_4^{2-}, forming strong coordination bonds (La/Zn-O-P). Previous studies indicated that the electronegativity gradient between La and Zn (Zn > La) drove internal charge transfer. The introduction of La and Zn in the oxide matrix induced internal charge transfer via surrounding O 2p ligands (e.g., Zn→La). Subsequently, La back-donated electrons into the O 2p* antibonding orbitals of HPO_4^{2-}. Consequently, the energy barrier for phosphate chemisorption was reduced, facilitating the formation of stable La/Zn···PO_4 species and synergistically improving adsorption kinetics and capacity (Khare et al., 2005).

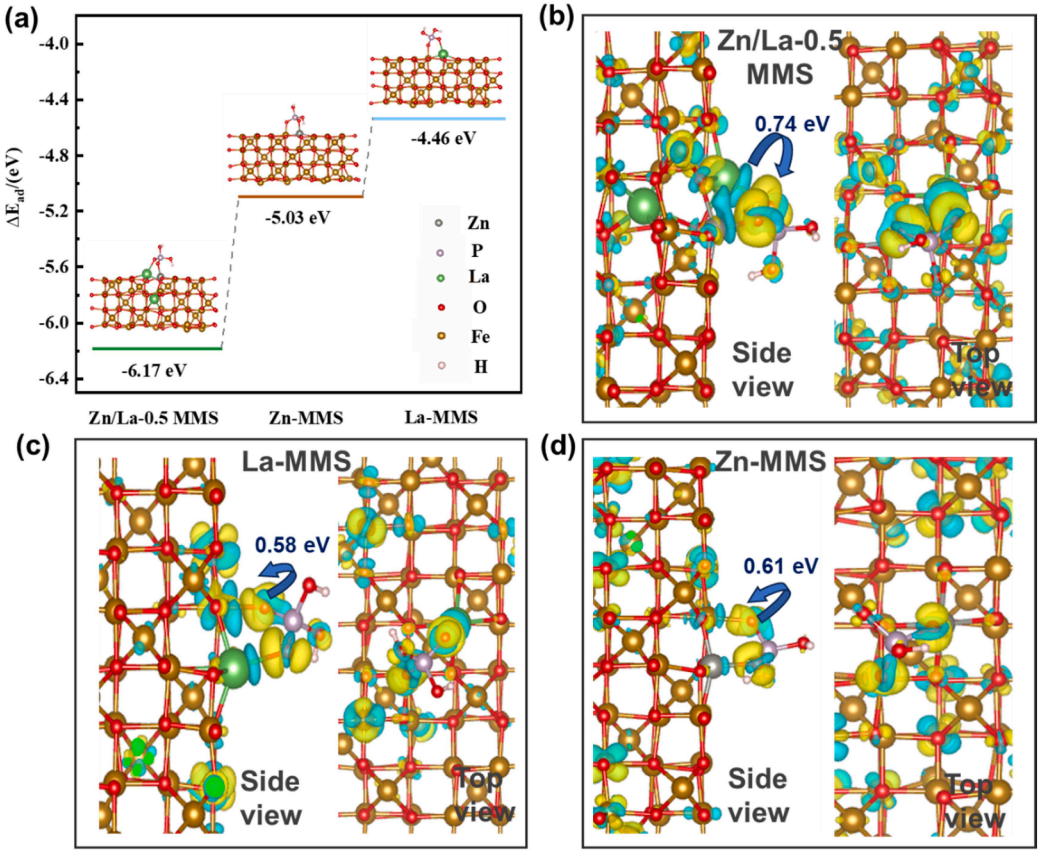

Fig. 8. (a) Phosphate adsorption energies; Side and top views of the charge density difference and Bader charge analysis on (b) Zn/La-0.5 MMS, (c) Zn-MMS, and (d) La-MMS (yellow regions indicate increased charge densities, while blue regions indicate reduced charge densities).

3.3.5. XAS analysis

X-ray absorption fine-structure (XAFS) spectroscopy was employed to trace the interfacial charge flow upon phosphate adsorption (Ravel and Newville, 2005). A set of four different kinds of samples, i.e., the pristine Zn/La MMS, the phosphate-adsorbed Zn/La MMS, the phosphate-adsorbed $La(OH)_3$ and the phosphate-adsorbed $Zn(OH)_2$, were characterized at the Zn K-edge and La L_3-edge under identical beamline conditions (Fig. 9).

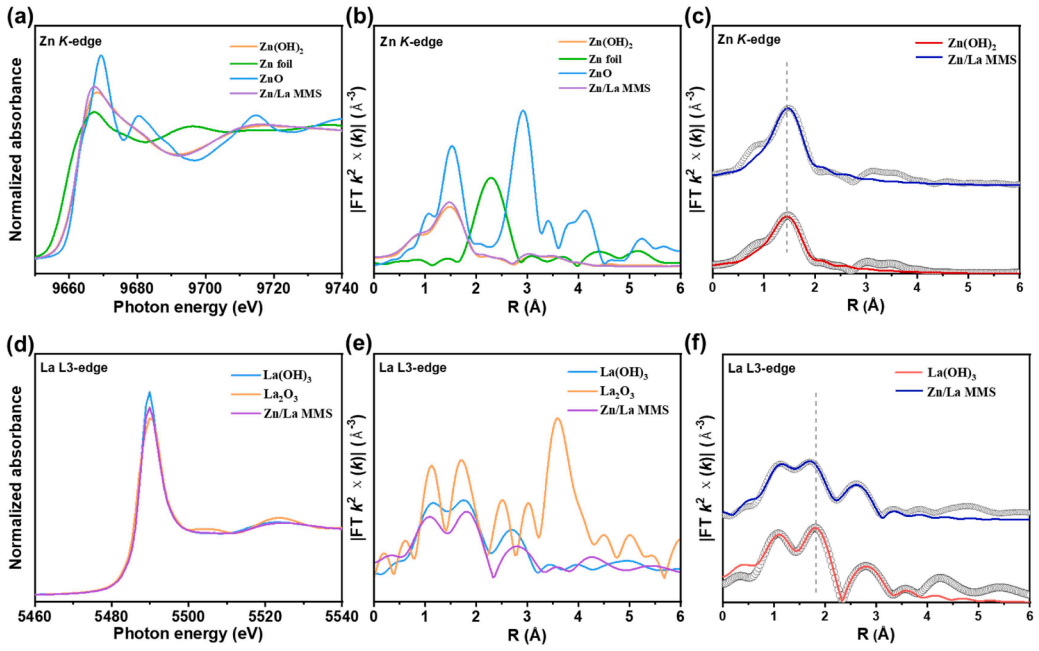

Fig. 9. (a) Zn K-edge XANES, (b) FT-EXAFS, and (c) R-space fitting for $Zn(OH)_2$ and Zn/La MMS; (d) La L_3-edge XANES, (e) FT-EXAFS, and (f) R-space fitting for La $(OH)_3$ and Zn/La MMS.

Relative to the respective oxide references, the Zn K-edge of Zn/La MMS exhibited a + 0.35 eV shift to the higher energy side (Fig. 9a), evidencing $Zn^{2+}\rightarrow Zn^{(+\delta)}$ oxidation (reduced 3d electron density) (Chen et al., 2023). Conversely, the La L_3-edge spectrum showed an −0.42 eV shift to the lower energy side (Fig. 9d), indicating $La^{3+}\rightarrow La^{(-\delta)}$ reduction (increased 5d electron density). Collectively these results demonstrated the migration of electron from Zn to La (i.e., interfacial electron redistribution).

Fourier-transformed k^2-weighted EXAFS spectra (Fig. 9c, f) showed a marginal change in the Zn-O bond length with the Zn coordination number decreasing slightly from 5.6 to 5.1, due to a fact that the fully occupied $3d^{10}$ shell of Zn was hardly affected by antibonding interactions (Trivedi et al., 2001). In contrast, the La-O bond length shortened significantly from 1.76 to 1.71 Å with its coordination number increasing from 3.4 to 4.0. This contraction are considered to be arose from electron back-donation from La into the O 2p* antibonding orbitals of phosphate, forming covalent La-O-P bonds, which thereby enhancing the synergistic adsorption capability of the bimetallic sites (Bejger et al., 2025). The specific fitting data were presented in Table S13.

4. Conclusions

This study developed a novel approach for the preparation of magnetic mesoporous microspheres (MMS) loading with Zn/La metal for advanced phosphate adsorption using simple etching and co-precipitation methods. Effective and highly efficient phosphate removal from wastewater was achieved owing to the bimetallic synergetic effect, the resultant enhanced adsorption, and the unique mesoporous structure. The resultant Zn/La-0.5 MMS adsorbent showed an approximately 15-fold increase in maximum adsorption capacity compared with the undoped MMS, with a maximum value of 140.9 mg P/g. Low residual TP (0.013 mg/L) concentrations were achieved for the treatment of real surface water. This material efficiently removed phosphate within a pH range of 3 to 11, with extremely low leaching of metals under actual application conditions. The adsorption of phosphate on the Zn/La-0.5 MMS was spontaneous and endothermic. Structural analysis and characterization results indicated that the adsorption of phosphate by the Zn/La-0.5 MMS was mainly achieved via inner-sphere complexation, ligand exchange, and intermolecular hydrogen bonding and electrostatic interactions on its surface. High phosphate adsorption performances sustained in solutions containing coexisting ions (Cl^-, NO_3^-, SO_4^{2-}, and HCO_3) or humic acids at concentrations 20 times and 50 times that of phosphate and within the actual water/wastewater matrix. After five cycles of regeneration and reuse, 79 % of its original phosphate adsorption capacity remained. DFT calculation together with differential charge density and Bader charge analyses revealed that reverse electron transfer occurred, where electron flow from the La/Zn-O hybridized orbitals into the unoccupied O 2p antibonding orbitals of HPO_4^{2-}, forming strong coordination bonds (La/Zn-O-P), rendering /La-0.5 MMS superior phosphate adsorption performance than mono-metallic systems (Zn MMS and La MMS). Overall, this study provided a simple and practical method for the development of highly efficient, reliable, stable, and readily separable and recoverable adsorbents for phosphate removal from water and wastewater.

CRediT authorship contribution statement

Fanglin He: Writing – original draft, Methodology, Investigation, Formal analysis, Conceptualization. **Ming Chang:** Writing – review & editing, Resources, Data curation. **Chaohai Wei:** Supervision, Project administration. **Feng Qian:** Writing – review & editing, Methodology. **Xuhan Deng:** Investigation, Methodology. **Guanglei Qiu:** Writing – review & editing, Supervision, Resources, Project administration, Investigation, Funding acquisition, Conceptualization.

Declaration of competing interest

The authors declare that they have no known competing financial interests or personal relationships that could have appeared to influence the work reported in this paper.

Acknowledgments

This research is supported by the National Natural Science Foundation of China (52270035 and 51808297), the Natural Science Foundation of Guangdong Province (2021A1515010494), the Guangzhou Key Research and Development Program (2023B03J1334 and 2025A04J7050), and the Pearl River Talent Recruitment Program (2019QN01L125).

Supplementary materials

Supplementary material associated with this article can be found, in the online version, at doi:10.1016/j.watres.2025.124753.

Data availability

I have shared the link to my data at the Attach File step.

References

Altaf, R., Sun, B., Lu, H., Zhao, H., Liu, D., 2023. Removal and recovery of phosphonates from wastewater via adsorption. Crit. Rev. Env. Sci. Technol. 53, 1032–1058. https://doi.org/10.1080/10643389.2022.2115271.

Beer, P.D., Gale, P.A., 2001. Anion recognition and sensing: the State of the art and future perspectives. Angew. Chem. Int. Ed. 40, 486–516. https://doi.org/10.1002/1521-3773(20010202)40:3%253C486::AID-ANIE486%253E3.0.CO;2-P.

Bejger, G.R., Caucci, M.K., Almishal, S.S.I., Yang, B., Maria, J.-P., Sinnott, S.B., Rost, C. M., 2025. Lanthanide L-edge spectroscopy of high-entropy oxides: insights into valence and phase stability. J. Mater. Chem. A 13, 29060–29069. https://doi.org/10.1039/D5TA03815D.

Chang, Y., Wei, Z., Chang, X., Ma, G., Meng, L., Liu, T., Yang, L., Guo, Y., Ma, X., 2021. Hollow hierarchically porous La_2O_3 with controllable multishells: a high-performance adsorbent for phosphate removal. Chem. Eng. J. 421, 127816. https://doi.org/10.1016/j.cej.2020.127816.

Chen, B., Zhao, H., Chen, S., Long, F., Huang, B., Yang, B., Pan, X., 2019a. A magnetically recyclable chitosan composite adsorbent functionalized with EDTA for simultaneous capture of anionic dye and heavy metals in complex wastewater. Chem. Eng. J. 356, 69–80. https://doi.org/10.1016/j.cej.2018.08.222.

Chen, D.T., Roy, A., Li, Y.Q., Bogush, A., Au, W.Y., Stegemann, J.A., 2023. Speciation of toxic pollutants in Pb/Zn smelter slags by X-ray absorption spectroscopy in the context of the literature. J. Hazard. Mater. 460, 132373. https://doi.org/10.1016/j.jhazmat.2023.132373.

Chen, L., Li, Y., Sun, Y., Chen, Y., Qian, J., 2019b. $La(OH)_3$ loaded magnetic mesoporous nanospheres with highly efficient phosphate removal properties and superior pH stability. Chem. Eng. J. 360, 342–348. https://doi.org/10.1016/j.cej.2018.11.234.

Cheng, K., Hou, M., Li, T., Qiao, Z., Liu, P., Ding, J., Sun, W., Li, Y., Gao, F., Li, X., Yang, M., 2024. Tracking the motion of an intruder particle in a three-dimensional granular bed on-board the Chinese Space Station. Microgravity Sci. Technol. 36, 15. https://doi.org/10.1007/s12217-024-10102-2.

Cui, R., Ma, J., Jiao, G., Sun, R., 2023. Efficient removal of phosphate from aqueous media using magnetic bimetallic lanthanum-iron-modified sulfonylmethylated lignin biochar. Int. J. Biol. Macromol. 247, 125809. https://doi.org/10.1016/j.ijbiomac.2023.125809.

Drenkova-Tuhtan, A., Schneider, M., Franzreb, M., Meyer, C., Gellermann, C., Sextl, G., Mandel, K., Steinmetz, H., 2017. Pilot-scale removal and recovery of dissolved phosphate from secondary wastewater effluents with reusable ZnFeZr adsorbent@Fe_3O_4/SiO_2 particles with magnetic harvesting. Water Res. 109, 77–87. https://doi.org/10.1016/j.watres.2016.11.039.

Elkhlifi, Z., Sellaoui, L., Zhao, M., Ifthikar, J., Jawad, A., Shahib, I.I., Sijilmassi, B., Lahori, A.H., Selvasembian, R., Meili, L., Gendy, E.A., Chen, Z., 2022. Lanthanum hydroxide engineered sewage sludge biochar for efficient phosphate elimination: mechanism interpretation using physical modelling. Sci. Total. Environ. 803, 149888. https://doi.org/10.1016/j.scitotenv.2021.149888.

Elser, J.J., 2012. Phosphorus: a limiting nutrient for humanity? Curr. Opin. Biotechnol. 23, 833–838. https://doi.org/10.1016/j.copbio.2012.03.001.

Frost, R.L., Locos, O.B., Ruan, H., Kloprogge, J.T., 2001. Near-infrared and mid-infrared spectroscopic study of sepiolites and palygorskites. Vib. Spectrosc. 27, 1–13. https://doi.org/10.1016/S0924-2031(01)00110-2.

Furusawa, T., Smith, J.M., 1974. Intraparticle mass transport in slurries by dynamic adsorption studies. AIChE J. 20, 88–93. https://doi.org/10.1002/aic.690200111.

Gao, Z., Wei, Y., Tian, X., Liu, Y., Lan, X., Zhang, D., Han, S., Huo, P., 2024. A novel Ce/Fe bimetallic metal-organic framework with ortho-dodecahedral multilevel structure

for enhanced phosphate adsorption. Chem. Eng. J. 486, 150284. https://doi.org/10.1016/j.cej.2024.150284.
He, J., Zhou, X., Xu, P., Sun, J., 2021. Promoting electrocatalytic water oxidation through tungsten-modulated oxygen vacancies on hierarchical FeNi-layered double hydroxide. Nano. Energy 80, 105540. https://doi.org/10.1016/j.nanoen.2020.105540.
Ho, Y., 2006. Review of second-order models for adsorption systems. J. Hazard. Mater. 136, 681–689. https://doi.org/10.1016/j.jhazmat.2005.12.043.
Khare, N., Hesterberg, D., Martin, J.D., 2005. XANES investigation of phosphate sorption in single and binary systems of iron and aluminum oxide minerals. Env. Sci. Technol. 39, 2152–2160. https://doi.org/10.1021/es049237b.
Kong, H., Wang, W., Wang, J., Zhang, G., Shen, F., Jiang, H., Li, Q., Huang, Z., 2024. New insights into lanthanum-calcium bimetal for phosphate removal: performance, molecular dynamics and life cycle assessment. Sep. Purif. Technol. 351, 128038. https://doi.org/10.1016/j.seppur.2024.128038.
Kong, L., Tian, Y., Pang, Z., Huang, X., Li, M., Yang, R., Li, N., Zhang, J., Zuo, W., 2019. Synchronous phosphate and fluoride removal from water by 3D rice-like lanthanum-doped La@MgAl nanocomposites. Chem. Eng. J. 371, 893–902. https://doi.org/10.1016/j.cej.2019.04.116.
Kresse, G., Furthmüller, J., 1996. Efficiency of ab-initio total energy calculations for metals and semiconductors using a plane-wave basis set. Comput. Mater. Sci. 6, 15–50. https://doi.org/10.1016/0927-0256(96)00008-0.
Lan, Z., Lin, Y., Yang, C., 2022. Lanthanum-iron incorporated chitosan beads for adsorption of phosphate and cadmium from aqueous solutions. Chem. Eng. J. 448, 137519. https://doi.org/10.1016/j.cej.2022.137519.
Li, D., Chen, M., Jiang, Y., 2025a. Adsorptive removal of phosphate by ZnAlLa ternary layered double hydroxides: synthesis conditions, adsorption performance, mechanism and reusability. Sep. Purif. Technol 354, 128668. https://doi.org/10.1016/j.seppur.2024.128668.
Li, F., Wu, W., Li, R., Fu, X., 2016. Adsorption of phosphate by acid-modified fly ash and palygorskite in aqueous solution: experimental and modeling. Appl. Clay. Sci. 132–133, 343–352. https://doi.org/10.1016/j.clay.2016.06.028.
Li, Z., Wei, Y., Wu, H., Yuan, P., Bu, H., Tan, X., 2025b. Efficient and sustainable phosphate removal and recovery from wastewater with zinc-substituted magnetite. Sep. Purif. Technol 360, 130642. https://doi.org/10.1016/j.seppur.2024.130642.
Liu, B., Nan, J., Jiang, R., Wu, F., Song, L., Ge, Z., Ye, X., Zhang, X., Wang, W., 2023. Three-dimensional porous aerogel-bead absorbent with high dispersibility of lanthanum active sites to boost phosphorus scavenging. Chem. Eng. J. 451, 138509. https://doi.org/10.1016/j.cej.2022.138509.
Liu, C., Wang, Y., Li, X., Li, J., Dong, S., Hao, H., Tong, Y., Zhou, Y., 2022. Highly efficient P uptake by Fe3O4 loaded amorphous Zr-La (carbonate) oxides: electrostatic attraction, inner-sphere complexation and oxygen vacancies acceleration effect. J. Environ. Sci. 120, 18–29. https://doi.org/10.1016/j.jes.2022.01.003.
Mahmoud, M.E., Obada, M.K., Nabil, G.M., 2024. Enhanced removing of phosphate ions from agricultural drainage wastewater by using microwave-assisted synthesized attapulgite (Fullers earth) @carboxymethylcellulose nanocomposite. Int. J. Biol. Macromol. 255, 128081. https://doi.org/10.1016/j.ijbiomac.2023.128081.
Mi, X., Yu, F., Zhang, H., Chen, R., Hu, X., Zhang, W., Wang, B., 2022. Lanthanum activated palygorskite for selective phosphate separation from aqueous media: comprehensive understanding of adsorptive behavior and mechanism affected by interfering substances. Chem. Eng. J. 443, 136423. https://doi.org/10.1016/j.cej.2022.136423.
Nakarmi, A., Bourdo, S.E., Ruhl, L., Kanel, S., Nadagouda, M., Kumar Alla, P., Pavel, I., Viswanathan, T., 2020. Benign zinc oxide betaine-modified biochar nanocomposites for phosphate removal from aqueous solutions. J. Env. Manage. 272, 111048. https://doi.org/10.1016/j.jenvman.2020.111048.
Nguyen, V.P., Nguyen, K.T.T., Ton, L.T., Nguyen, D.T., Nguyen, K.Q., Vu, M.T., Tran, H. N., 2020. Dual-electronic nanomaterial (Synthetic Clay) for effective removal of toxic cationic and oxyanionic metal ions from water. J. Nanomater. 2020, 1–11. https://doi.org/10.1155/2020/1783749.
Peng, J., Wu, E., Wang, N., Quan, X., Sun, M., Hu, Q., 2019. Removal of sulfonamide antibiotics from water by adsorption and persulfate oxidation process. J. Mol. Liq. 274, 632–638. https://doi.org/10.1016/j.molliq.2018.11.034.
Perdew, J.P., Burke, K., Ernzerhof, M., 1996. Generalized gradient approximation made simple. Phys. Rev. Lett. 77, 3865–3868. https://doi.org/10.1103/PhysRevLett.77.3865.
Ravel, B., Newville, M., 2005. ATHENA, ARTEMIS, HEPHAESTUS : data analysis for X-ray absorption spectroscopy using IFEFFIT. J. Synchrotron. Rad. 12, 537–541. https://doi.org/10.1107/S0909049505012719.
Salinas, T., Durruty, I., Arciniegas, L., Pasquevich, G., Lanfranconi, M., Orsi, I., Alvarez, V., Bonanni, S., 2018. Design and testing of a pilot scale magnetic separator for the treatment of textile dyeing wastewater. J. Env. Manage. 218, 562–568. https://doi.org/10.1016/j.jenvman.2018.04.096.
Sanville, E., Kenny, S.D., Smith, R., Henkelman, G., 2007. Improved grid-based algorithm for Bader charge allocation. J. Comput. Chem. 28, 899–908. https://doi.org/10.1002/jcc.20575.
Song, S.-J., Raja, I.S., Lee, Y.B., Kang, M.S., Seo, H.J., Lee, H.U., Han, D.-W., 2019. Comparison of cytotoxicity of black phosphorus nanosheets in different types of fibroblasts. Biomater. Res. 23, 23. https://doi.org/10.1186/s40824-019-0174-x.
Spears, B.M., Lürling, M., Yasseri, S., Castro-Castellon, A.T., Gibbs, M., Meis, S., McDonald, C., McIntosh, J., Sleep, D., Van Oosterhout, F., 2013. Lake responses following lanthanum-modified bentonite clay (Phoslock®) application: an analysis of water column lanthanum data from 16 case study lakes. Water Res. 47, 5930–5942. https://doi.org/10.1016/j.watres.2013.07.016.
Sun, E., Zhang, Y., Xiao, Q., Li, H., Qu, P., Yong, C., Wang, B., Feng, Y., Huang, H., Yang, L., Hunter, C., 2022. Formable porous biochar loaded with La-Fe(hydr)oxides/montmorillonite for efficient removal of phosphorus in wastewater: process and mechanisms. Biochar 4, 53. https://doi.org/10.1007/s42773-022-00177-8.
Surendranath, Y., Kanan, M.W., Nocera, D.G., 2010. Mechanistic studies of the oxygen evolution reaction by a cobalt-phosphate catalyst at neutral pH. J. Am. Chem. Soc. 132, 16501–16509. https://doi.org/10.1021/ja106102b.
Thijs, L.C., Kuerten, J.G.M., Zeegers, J.C.H., Tajfirooz, S., 2023. Magnetic density separation of particles in honeycomb-generated wake turbulence. Chem. Eng. Sci. 278, 118930. https://doi.org/10.1016/j.ces.2023.118930.
Trivedi, P., Axe, L., Tyson, T.A., 2001. XAS studies of Ni and Zn sorbed to hydrous manganese oxide. Env. Sci. Technol. 35, 4515–4521. https://doi.org/10.1021/es0109848.
Wang, C., Auad, M.L., Marcovich, N.E., Nutt, S., 2008. Synthesis and characterization of organically modified attapulgite/polyurethane nanocomposites. J. Appl. Polym. Sci. 109, 2562–2570. https://doi.org/10.1002/app.28254.
Wang, W., Kong, H., Wang, J., Zhang, G., Shen, F., Liu, F., Huang, Z., 2024a. Lanthanum-calcium bimetallic-modified attapulgite- chitosan hydrogel beads for efficient phosphate removal from water: performance evaluation, mechanistic and life cycle assessment. Carbohydr. Polym 338, 122183. https://doi.org/10.1016/j.carbpol.2024.122183.
Wang, Z., Su, J., Zhao, T., Li, J., Zhang, L., 2024b. Enhanced removal of fluoride from groundwater using biosynthetic hydroxyapatite modified by bimetallic (La–Fe or La–Al) hydroxides. J. Clean. Prod 436, 140649. https://doi.org/10.1016/j.jclepro.2024.140649.
Wu, L., Yu, L., Zhang, F., Wang, D., Luo, D., Song, S., Yuan, C., Karim, A., Chen, S., Ren, Z., 2020. Facile synthesis of nanoparticle-stacked tungsten-doped nickel iron layered double hydroxide nanosheets for boosting oxygen evolution reaction. J. Mater. Chem. A 8, 8096–8103. https://doi.org/10.1039/D0TA00691B.
Xia, S., Luo, Q., Liu, J., Yang, X., Lei, J., Shao, J., Tang, X., 2024. In situ spontaneous construction of zinc phosphate coating layer toward highly reversible zinc metal anodes. Small 20, 2310497. https://doi.org/10.1002/smll.202310497.
Xiang, C., Wang, H., Ji, Q., Zhang, G., Qu, J., 2019. Tracking internal electron shuttle using X-ray spectroscopies in La/Zr hydroxide for reconciliation of charge-transfer interaction and coordination toward phosphate. ACS. Appl. Mater. Interfaces 11, 24699–24706. https://doi.org/10.1021/acsami.9b05397.
Yan, J., Jiang, T., Yao, Y., Lu, S., Wang, Q., Wei, S., 2016. Preliminary investigation of phosphorus adsorption onto two types of iron oxide-organic matter complexes. J. Environ. Sci. 42, 152–162. https://doi.org/10.1016/j.jes.2015.08.008.
Yang, B., Zhang, X., Shrimant, B., Kulkarni, T., Kumar, R., Arges, C.G., 2024. Selective phosphate removal with manganese oxide composite anion exchange membranes in membrane capacitive deionization. Chem. Eng. J. 495, 153468. https://doi.org/10.1016/j.cej.2024.153468.
Yang, Y., Dang, L., Shearer, M.J., Sheng, H., Li, W., Chen, J., Xiao, P., Zhang, Y., Hamers, R.J., Jin, S., 2018. Highly active trimetallic NiFeCr layered double hydroxide electrocatalysts for oxygen evolution reaction. Adv. Energy Mater. 8, 1703189. https://doi.org/10.1002/aenm.201703189.
Yi, Y., Fu, Y., Wang, Y., Xu, Z., Diao, Z., 2024. Lanthanum/iron co-modified biochar for highly efficient adsorption of low-concentration phosphate from aqueous solution. J. Environ. Chem. Eng. 12, 111876. https://doi.org/10.1016/j.jece.2024.111876.
Yin, X., Li, X., Petropoulos, E., Feng, Y., Yang, B., Xue, L., Yang, L., He, S., 2022. Phosphate removal from actual wastewater via $La(OH)_3$-C_3N_4 adsorption: performance, mechanisms and applicability. Sci. Total. Environ. 814, 152791. https://doi.org/10.1016/j.scitotenv.2021.152791.
Yu, L., Ma, L., Zhu, N., Ren, Y., 2025. Enhanced phosphate adsorption in low-concentration solutions using La/Zr hydroxide-modified diatomite: mechanisms and efficiency. Sep. Purif. Technol. 372, 133422. https://doi.org/10.1016/j.seppur.2025.133422.
Yuh-Shan, H., 2004. Citation review of Lagergren kinetic rate equation on adsorption reactions. Scientometrics 59, 171–177. https://doi.org/10.1023/B:SCIE.0000013305.99473.cf.
Zhai, P., Xia, M., Wu, Y., Zhang, G., Gao, J., Zhang, B., Cao, S., Zhang, Y., Li, Z., Fan, Z., Wang, C., Zhang, X., Miller, J.T., Sun, L., Hou, J., 2021. Engineering single-atomic ruthenium catalytic sites on defective nickel-iron layered double hydroxide for overall water splitting. Nat. Commun. 12, 4587. https://doi.org/10.1038/s41467-021-24828-9.
Zhang, B., Xu, L., Zhao, Z., Peng, S., Yu, C., Zhang, X., Zong, Y., Wu, D., 2022. Enhanced phosphate removal by nano-lanthanum hydroxide embedded silica aerogel composites: superior performance and insights into specific adsorption mechanism. Sep. Purif. Technol. 285, 120365. https://doi.org/10.1016/j.seppur.2021.120365.
Zhang, X., Sun, F., He, J., Xu, H., Cui, F., Wang, W., 2017. Robust phosphate capture over inorganic adsorbents derived from lanthanum metal organic frameworks. Chem. Eng. J. 326, 1086–1094. https://doi.org/10.1016/j.cej.2017.06.052.
Zhang, Y., Akindolie, M.S., Tian, X., Wu, B., Hu, Q., Jiang, Z., Wang, L., Tao, Y., Cao, B., Qu, J., 2021. Enhanced phosphate scavenging with effective recovery by magnetic porous biochar supported $La(OH)_3$: kinetics, isotherms, mechanisms and applications for water and real wastewater. Bioresour. Technol. 319, 124232. https://doi.org/10.1016/j.biortech.2020.124232.
Zhu, Z., Qin, L., Liu, Y., Zhang, Q., Cheng, P., Liang, W., 2024a. Fabrication and mechanism of La/Al bimetallic organic frameworks for phosphate removal. Chem. Eng. J. 479, 147081. https://doi.org/10.1016/j.cej.2023.147081.
Zhu, Z., Qin, L., Liu, Y., Zhang, Q., Cheng, P., Liang, W., 2024b. Fabrication and mechanism of La/Al bimetallic organic frameworks for phosphate removal. Chem. Eng. J. 479, 147081. https://doi.org/10.1016/j.cej.2023.147081.